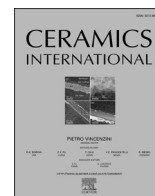




Contents lists available at ScienceDirect

Ceramics International

journal homepage: [www.elsevier.com/locate/ceramint](http://www.elsevier.com/locate/ceramint)

# Synthesis and characterization of Sr<sup>2+</sup> and Gd<sup>3+</sup> doped magnetite nanoparticles for magnetic hyperthermia and drug delivery application

Sunday J. Olusegun<sup>a,\*</sup>, Magdalena Osial<sup>b</sup>, Agnieszka Majkowska-Pilip<sup>c</sup>,  
Kinga Źelechowska-Matysiak<sup>c</sup>, Dorota Nieciecka<sup>a</sup>, Michal Krajewski<sup>a</sup>, Marek Pękała<sup>a</sup>,  
Pawel Kryszynski<sup>a,\*\*</sup>

<sup>a</sup> Faculty of Chemistry, University of Warsaw, Pasteur Street 1, 02-093, Warsaw, Poland

<sup>b</sup> Department of the Theory of Continuous Media, Institute of Fundamental Technological Research, Polish Academy of Sciences, Pawlinskiego 5B Street, 02-106, Warsaw, Poland

<sup>c</sup> Centre of Radiochemistry and Nuclear Chemistry, Institute of Nuclear Chemistry and Technology, Dorodna 16 Str, 03-195, Warsaw, Poland

## ARTICLE INFO

Handling Editor: Dr P. Vincenzini

### Keywords:

Magnetic hyperthermia  
Iron oxides  
Drug delivery  
Gadolinium  
Strontium

## ABSTRACT

Commendable efforts have been gingered towards the fight against cancer. Nevertheless, it remains a major public health concern due to its predominant cause of death globally. Given this, we synthesized two different nanoparticles, Sr<sup>2+</sup> and Gd<sup>3+</sup> doped magnetite for magnetic hyperthermia and drug delivery application. Based on the characterization, the diffractogram shows that only one phase related to magnetite with a crystallite size of 10 nm was formed. TEM images revealed nanoparticles of spherical shapes of approximately 12 nm. There is no difference in magnetic saturation of the as-received synthesized samples (Fe<sub>3</sub>O<sub>4</sub>@Sr and Fe<sub>3</sub>O<sub>4</sub>@Gd), while the BET-specific surface area of Fe<sub>3</sub>O<sub>4</sub>@Gd is 8 m<sup>2</sup> g<sup>-1</sup> higher than Fe<sub>3</sub>O<sub>4</sub>@Sr. The heat generation in alternating magnetic field (the magnetic hyperthermia) of Fe<sub>3</sub>O<sub>4</sub>@Sr functionalized with citric acid and loaded with 5-fluorouracil (Fe<sub>3</sub>O<sub>4</sub>@Sr@CA@5-flu) is slower than Fe<sub>3</sub>O<sub>4</sub>@Gd@CA@5-flu. The specific absorption rate (SAR) of Fe<sub>3</sub>O<sub>4</sub>@Gd@CA@5-flu, 112.0 ± 10.4 W g<sup>-1</sup> was found to be higher than that of Fe<sub>3</sub>O<sub>4</sub>@Sr@CA@5-flu. The thermogram shows that 11% of the drug was successfully loaded on Fe<sub>3</sub>O<sub>4</sub>@Gd@CA@5-flu. The release of the antitumor drug by the synthesized nanoparticle drug carriers for ovarian cancer (SKOV-3 cells) therapy showed that more than 50% of the cancer cell's viability was reduced after 72 h of incubation. The synthesized nanoparticles demonstrated a promising drug carrier for the treatment of SKOV-3 cells.

## 1. Introduction

Cancer is rated as one of the major causes of death worldwide and has been seen as an acute condition that consists of infected and normal cell types, which has limited single-mode treatment to combat its high heterogeneity at both initial and advanced stages [1,2]. The consequential death that cancer brought on humanity has necessitated proactive measures directed toward its treatment, resulting in the development of new therapeutic strategies. Sad to note, due to the heterogeneity of patients and resistance of cancer towards therapy, this has resulted in poor treatment outcomes and severe side effects on the patients [1]. Therefore, optimizing treatment options that could be more efficacious and yield the highest results is of utmost importance. The quest for these has awakened the curiosity of researchers from different

related fields [3]. This will go in a long way to bring hope, comfort, and reassurance and to minimize the distress that could weaken the immune defense system of cancer patients [4].

However, the treatment of cancer, which commonly involves surgery and radiation among others, has harmful consequences on healthy tissues [5,6]. Given these challenges, efforts have been directed toward the minimization of the adverse effects of cancer therapy through the usage of drugs. Meanwhile, the traditional means of administering drugs into the body system which entails swallowing a pill or intravenous in which the drug is dispersed throughout the body system and eventually reaches the affected organ for healing has a major disadvantage in that the healthy parts of the body could be adversely affected in the process of dispersion [7]. Targeted drug delivery in which a therapeutic agent (drug) is being introduced into the tumor cell is presently employed as a

\* Corresponding author.

\*\* Corresponding author.

E-mail addresses: [o.sunday@chem.uw.edu.pl](mailto:o.sunday@chem.uw.edu.pl) (S.J. Olusegun), [pakrys@chem.uw.edu.pl](mailto:pakrys@chem.uw.edu.pl) (P. Kryszynski).

<https://doi.org/10.1016/j.ceramint.2023.03.102>

Received 22 December 2022; Received in revised form 7 March 2023; Accepted 10 March 2023

Available online 11 March 2023

0272-8842/© 2023 Elsevier Ltd and Techna Group S.r.l. All rights reserved.

replacement for traditional methods of administering drugs for cancer therapy.

A drug delivery system, a better route to dispense drugs into the body system has many benefits (greater efficiency, increased security, lower cytotoxicity, controlled release, targeted drug delivery, and improved stability) over the traditional forms [8,9]. It helps to prevent the wastage of drugs by transportation to the targeted tissues and enhances treatment safety [10]. As much as the drug delivery system helps to curb the menace that is accompanied by the traditional form of therapy, another huge task is to be able to deliver the exact amount of the drug to the target cell without causing any side effects [11]. Therefore, targeting drugs to affected cells through nano-drug delivery systems has reduced to a significant level the associated side effects of drugs toward cancer treatment [12]. It was stated that a drug delivery system at the nanoscale is a promising way of administering drugs to a targeted cell due to its enhancement of permeability and retention effect of solid tumors [13]. There is an increasing trend in the applications of nanoparticles in the biomedical sector, with the possible advantages of diagnosis, treatment of cancer cells, and monitoring of therapy. Nanoparticles as drug carriers have many advantages which include reduced toxic effect, increased solubility of the drug, prolonged time of drug retention in the site of the affected cell, and accurate targeting [12].

Meanwhile, it is important to adequately guide anticancer agents to the targeted cancer cell. This then brought the introduction of magnetic nanoparticles. Among the active drug delivery strategies, magnetic nanoparticles have gained more popularity because of the simple preparation methods, low cost, and easy modification. The use of iron oxide (superparamagnetic) nanoparticles for drug delivery, diagnosis, and treatment of cancer has gained wider recognition in biomedical applications [14]. One feature that makes superparamagnetic nanoparticles an interesting drug carrier is that they can be targeted to the affected tumor by an external magnet [15].

This research is designed to further strengthen efforts towards cancer therapy through the applications of drug delivery system which encompasses the usage of  $Gd^{3+}$  and  $Sr^{2+}$  doped magnetite. These two elements can be converted to their respective radioisotopes and used for medical applications [16]. Strontium (Sr), has been discovered to increase the formation of bone, and decrease the tendency of bone resorption and the possibility of risk of fractures [17]. While gadolinium contrast medium is used in magnetic resonance imaging [18]. In addition, lanthanide-doped nanomaterials, especially UCNPs (upconversion nanoparticles) have been attested to be good materials for both drug and gene delivery, image-guided agents, and photodynamic therapy [19]. Superparamagnetic iron oxide nanoparticles are nontoxic, can be modified with both organic and inorganic compounds, and have a promising method of being heat sources in magnetic hyperthermia [15]. Incorporating  $Sr^{2+}$  and  $Gd^{3+}$  into the core of superparamagnetic iron oxides could allow simultaneous hyperthermia and radiation therapy of the targeted tumor tissue, when loaded with a cancer drug, it could lead to the combination of hyperthermia, radiation, and drug release through an extrinsic energy source [20]. Overall, effective treatment of the tumor will be achieved.

## 2. Materials and methods

### 2.1. Materials

Iron(II)chloride tetrahydrate ( $FeCl_2 \cdot 4H_2O$ ), Iron(III)chloride hexahydrate ( $FeCl_3 \cdot 6H_2O$ ), ammonium hydroxide (25%  $NH_3$ , assay 99.99%), and 5-fluorouracil were purchased from Sigma-Aldrich. Strontium chloride and Gadolinium(III) chloride, were purchased from WARCHEM, Poland. Deionized water with a resistivity of 18.2  $M\Omega \text{ cm}$  was used throughout the experiments.

### 2.2. Synthesis of magnetite nanocomposites

$Fe_3O_4@Sr$  was synthesized as follows: 0.2 M of  $FeCl_3 \cdot 6H_2O$ , 0.0975 M of  $FeCl_2 \cdot 4H_2O$  and 0.0025 M of  $SrCl_2$ , were thoroughly mixed inside a 250 mL beaker to ensure total dissolution of the salts. Ammonium hydroxide was added to precipitate the desired products  $Fe_3O_4@Sr$  at alkaline pH. The precipitate ( $Fe_3O_4@Sr$ ) was heated to 90 °C for 1 h, and washed until pH is 7. The same steps were used for the production of  $Fe_3O_4@Gd$ , but the concentration of the respective salts are: 0.195 M of  $FeCl_3 \cdot 6H_2O$ , 0.1 M of  $FeCl_2 \cdot 4H_2O$  and 0.005 M of  $GdCl_3$ . In the first synthesis,  $Sr^{2+}$  was to substitute  $Fe^{2+}$ , while  $Gd^{3+}$  was to substitute  $Fe^{3+}$ . In both cases the molar percentage of the dopant was 2.5. This was chosen based on the previous work from our group [15].

### 2.3. Modifications of $Fe_3O_4@Sr$ and $Fe_3O_4@Gd$ with citric acid

The importance of the modification with surfactant is to prevent agglomeration of the nanoparticles during medical (drug delivery) application. Approximately, 400 mg of each nanoparticle ( $Fe_3O_4@Sr$  and  $Fe_3O_4@Gd$ ) was added to 100 mL of 0.05 M of citric acid. The pH of the suspension was adjusted to 5.2, thereafter heated to 80 °C and mechanically stirred for 3 h. The nanoparticles were washed thoroughly with acetone to remove excess citric acid and precipitate the nanoparticles. Thereafter the named Sr-doped iron oxide nanoparticles, functionalized with citric acid ( $Fe_3O_4@Sr@CA$ ), and named Gd-doped iron oxide nanoparticles, functionalized with citric acid ( $Fe_3O_4@Gd@CA$ ), were loaded with the drug.

### 2.4. Loading of the nanoparticles with drug

The following step was the adsorption of 5-fluorouracil onto the nanoparticles stabilized with citrates. Therefore, the 20 mL of colloidal suspension containing 400 mg of magnetic particles coated with citrates (mass estimated for non-stabilized nanoparticles) was placed in the beaker and vigorously stirred at 600 rpm for 5 min. Then, 20 mg of 5-fluorouracil was added, and the suspension was continuously stirred for 12 h at room temperature. Next, the stirring bar was removed from the suspension, and a beaker was placed in water with a temperature of about 3–6 °C (water was cooled down with ice cubes) continuously stirred with 100 rpm for 15 min, and then left for the subsequent cooling for 60 min without stirring. To check the stability of the suspension, it was put in the 50 mL in volume Falcon vial and centrifuged with a rotation rate of about 9,000 rpm for 30 min with cooling mode and, after that, collected on a magnet. Here, 1 mL of the supernatant from the top of the falcon vial was taken for UV–vis studies to check if the drug was fully adsorbed on the surface of the magnetic carrier. As the 5-fluorouracil was fully adsorbed, the suspension was shaken intensively on the orbital spinner for 5 min, and it was used for analyses. The same procedure was used for the adsorption of the drug on  $Fe_3O_4@Gd@CA$  nanoparticles. Despite the high stability of the suspensions, according to the in vitro studies of the magnetic drug carrier, it was not centrifuged to reduce the risk of the formation of aggregates even on a small scale, which could lead to the non-homogeneous distribution of nanoparticles on the tested cell cultures.

### 2.5. Interaction with biomimetic membranes

Langmuir monolayers were prepared using KSV Nima trough (Biolin Scientific, Sweden). The instrument was controlled by a PC using Nima LB software (v. 3.7). To prepare monolayers we used a mixture of lipids: DOPC (1,2-dioleoyl-sn-glycero-3-phosphocholine): DOPS (1,2-dioleoyl-sn-glycero-3-phospho-L-serine -sodium salt) in molar ratio 8:2. The lipid mixture was dissolved in chloroform to a final concentration of 2 mg  $mL^{-1}$ . Using a Hamilton microsyringe a 30  $\mu L$  sample of this solution was deposited onto the surface of the aqueous subphase in the trough and left for 10 min to allow the chloroform to evaporate. Next, the lipid

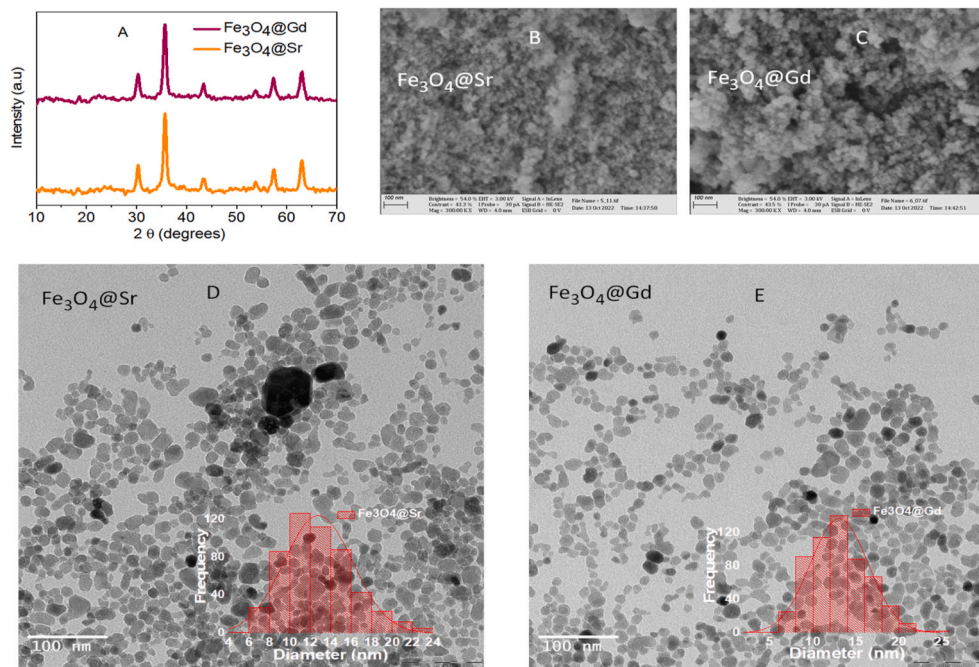


Fig. 1. The XRD (A), SEM (B and C), and TEM images (D and E) of the synthesized  $\text{Fe}_3\text{O}_4@\text{Sr}$  and  $\text{Fe}_3\text{O}_4@\text{Gd}$ .

molecules on the surface of the subphase were compressed continuously at a rate of  $10 \text{ cm}^2 \text{ min}^{-1}$  to record the pressure–area isotherms and form a monolayer. The same procedure was used to follow the nanoconjugates' interactions with lipid monolayers; in this case, the water subphase contained various concentrations of nanoparticles or conjugates, as specified later in the text.

## 2.6. In vitro cytotoxicity evaluation

One day before adding the compounds ( $\text{Fe}_3\text{O}_4 @\text{Gd}$ ,  $\text{Fe}_3\text{O}_4@\text{Gd}@\text{CA}$ ,  $\text{Fe}_3\text{O}_4@\text{Gd}@\text{CA}@5\text{-flu}$ , 5-flu), SKOV-3 cells ( $2.5 \times 10^3$  per well) were seeded in 96-wellplates. On the day of treatment initiation, the medium was replaced and the cells were incubated for 24 h, 48 h, and 72 h at  $37^\circ\text{C}$  and 5%  $\text{CO}_2$ . The wells were then rinsed with PBS and MTS reagent was added to the fresh medium. After 2 h of incubation, absorbance was measured at 490 nm.

## 2.7. Statistical analysis

The cytotoxicity test was repeated three times ( $n = 3$ ) in six replicates. The mean and standard deviation of the measurements were

calculated. GraphPad Prism v. 8.0 software (GraphPad Software Inc., San Diego, CA, USA) was used for statistical analysis. Values between groups ( $\text{Fe}_3\text{O}_4@\text{Gd}$  vs.  $\text{Fe}_3\text{O}_4@\text{Gd}@\text{CA}$ ,  $\text{Fe}_3\text{O}_4@\text{Gd}$  vs.  $\text{Fe}_3\text{O}_4@\text{Gd}@\text{CA}@5\text{-flu}$ ,  $\text{Fe}_3\text{O}_4@\text{Gd}@\text{CA}$  vs.  $\text{Fe}_3\text{O}_4@\text{Gd}@\text{CA}@5\text{-flu}$ , 5-flu vs.  $\text{Fe}_3\text{O}_4@\text{Gd}@\text{CA}@5\text{-flu}$ ) were compared using two-way ANOVA. Statistical significance was considered if  $p \leq 0.05$  (\*),  $p \leq 0.01$  (\*\*),  $p \leq 0.001$  (\*\*\*) and  $p \leq 0.0001$  (\*\*\*\*).

## 2.8. Characterization

Powder X-ray powder diffraction (XRD) was carried out on Bruker D8 Advance with DIFFRAC PLUS, Bruker - AXS GmbH 2000, software, at room temperature with a  $\text{Cu K}\alpha$  X-ray line  $\lambda = 1.544 \text{ \AA}$ , in the  $2\theta$  range from  $10$  to  $70^\circ$ . Transmission electron microscopy (TEM), Zeiss Libra 120 Plus, Stuttgart, operating at 120 kV was used for the identification and range of the particles' distribution. Scanning electron microscope (SEM), Merlin, manufactured by Zeiss, equipped with a Gemini II column operated in a low kV value range (0.5–1.5 kV), and probe current 10–20  $\mu\text{A}$ , was used to examine the morphology. The FTIR spectra between  $400 \text{ cm}^{-1}$  and  $4000 \text{ cm}^{-1}$  were collected on ThermoFisher Scientific Nicolet 8700 spectrometer through the use of the standard KBr

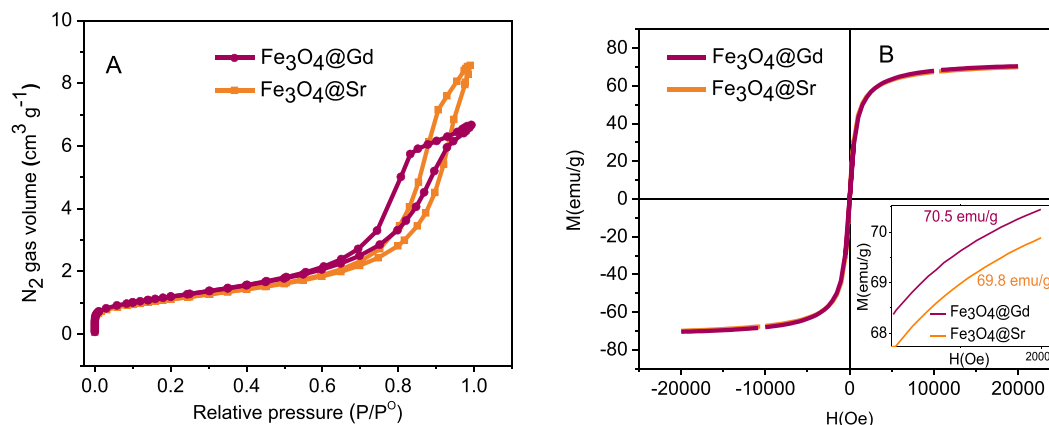


Fig. 2. The  $\text{N}_2$  adsorption-desorption (a), and magnetic saturation (b) of  $\text{Fe}_3\text{O}_4@\text{Sr}$  and  $\text{Fe}_3\text{O}_4@\text{Gd}$ .

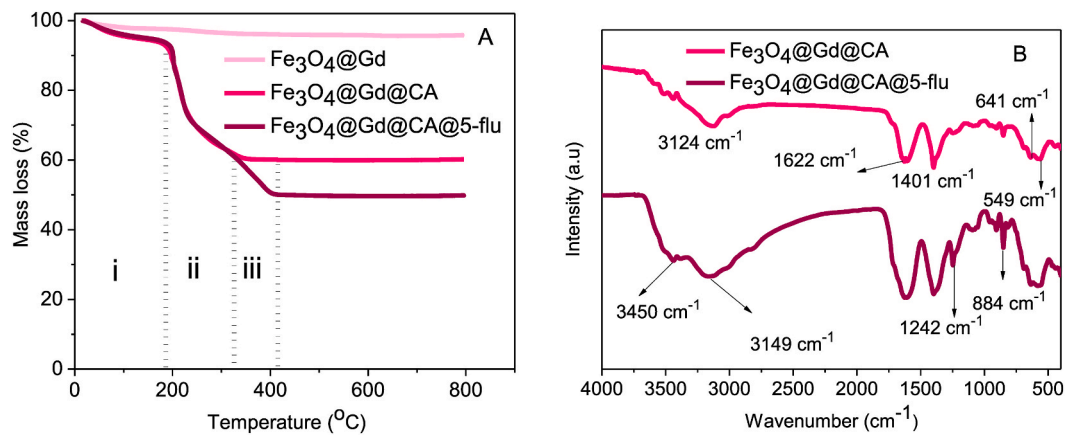


Fig. 3. The thermogram (A) and IR spectra (B) of  $\text{Fe}_3\text{O}_4$  doped gadolinium nanoparticles.

pellet method. The magnetic properties of the nanoparticles were investigated with a QD vibrating sample magnetometer (VSM) under the magnetic field ranging from  $-2.0$  T to  $+2.0$  T at a temperature of 100 K and 300 K with an accuracy of ca. 0.01 K. The  $\text{N}_2$  adsorption/desorption experiments were conducted on Micromeritics® ASAP 2060 apparatus at 77.349 K absolute temperature in the relative pressure range of 0.01–0.995  $p/p^0$ . Adsorption/desorption isotherm analysis was performed on ASAP 2060 software, by calculating the specific surface area using the BET method, distribution of pores, and their volumes. A thermogravimetric analyzer, TGA Q50 (TA Instruments), New Castle, PA, USA, was used to determine the mass loss. This was performed under nitrogen at  $60 \text{ cm}^3 \text{ min}^{-1}$  flow and oxygen at a  $5 \text{ cm}^3 \text{ min}^{-1}$  flow rate.

### 3. Results and discussion

#### 3.1. Characterization

The diffractogram of the synthesized nanoparticles is shown in Fig. 1A. It matches with the magnetite of ICSD No: 026410, having cubic cell and Fd-3m space group. Compare to the previously synthesized magnetite as reported in our group [15], there is no addition of a new phase which could be due to the presence of strontium and gadolinium. Based on the Scherrer equation, the crystallite size at  $2\theta$ ,  $35.6^\circ$  was calculated to be 10 nm. The surface morphology of the nanoparticles as revealed by scanning electron microscope shows agglomeration of particles Fig. 1B and C. Further insight into the distribution of the particles size was obtained from TEM images Fig. 1 D and E, which show nanoparticles of well-defined round shape, whose average particles size as obtained from the histogram (insert) is around 12 nm for both  $\text{Fe}_3\text{O}_4$ @Sr and  $\text{Fe}_3\text{O}_4$ @Gd.

The  $\text{N}_2$  adsorption-desorption of  $\text{Fe}_3\text{O}_4$ @Sr and  $\text{Fe}_3\text{O}_4$ @Gd are shown in Fig. 2A. The isotherm of  $\text{Fe}_3\text{O}_4$ @Sr is type II, a characteristic of non-porous materials in which the adsorption of the  $\text{N}_2$  gas did not reach a limit at  $p/p^0 = 1$ . The hysteresis is type H3, and the loop is typical of loose aggregates of particles that formed slit pores of no uniform shape [21,22]. The isotherm and hysteresis of  $\text{Fe}_3\text{O}_4$ @Gd are type-IV and H1-2 respectively. The BET-specific surface area of  $\text{Fe}_3\text{O}_4$ @Sr is  $89 \text{ m}^2 \text{ g}^{-1}$ , while that of  $\text{Fe}_3\text{O}_4$ @Gd is  $97 \text{ m}^2 \text{ g}^{-1}$ . The slight difference could be an assumption that Gd substituted for Fe. However, the difference is not so alarming that could prompt detailed investigation. The diameter of pores formed from the loose aggregation of the nanoparticles is between 10 and 20 nm for  $\text{Fe}_3\text{O}_4$ @Sr and 7–12 nm for  $\text{Fe}_3\text{O}_4$ @Gd. The pore distribution of  $\text{Fe}_3\text{O}_4$ @Gd was more uniform and a bit smaller in diameter this might be the reason for the transition from type-II/H3 to one more resembling a type-IV/H1-2.

The magnetization curve of the obtained nanoparticles ( $\text{emu g}^{-1}$ ) vs applied magnetic field (Oe) is displayed in Fig. 2B. The magnetic

saturation of the two samples is almost the same (see inset in Fig. 2B for enlargement). The obtained values of  $M_s$  for both samples are close to each other ( $\text{Fe}_3\text{O}_4$ @Gd:  $70.5 \text{ emu g}^{-1}$  and  $\text{Fe}_3\text{O}_4$ @Sr ( $69.8 \text{ emu g}^{-1}$ )), even though  $\text{Gd}^{2+}$  has 7 unpaired electrons in its 4f shell. This suggests that at the dopant level of 2.5%, the magnetic behavior of both samples is determined mainly by the magnetite core structure. Although it was expected that the  $M_s$  of  $\text{Fe}_3\text{O}_4$ @Gd would be higher than that of  $\text{Fe}_3\text{O}_4$ @Sr due to the presence of 7 unpaired electrons in its 4f shell electronic structure, this did not occur with the as-synthesized sample.

Therefore, to satisfy our curiosity, the two samples were heated to  $500^\circ\text{C}$ , and the magnetic saturation ( $M_s$ ) was thereafter measured again. The results are shown in the supplementary (Fig. S1), while  $\text{Fe}_3\text{O}_4$ @Sr nanoparticles completely lost their magnetic properties,  $\text{Fe}_3\text{O}_4$ @Gd retain its own with an up  $M_s$  value of  $54 \text{ emu g}^{-1}$ . More so, Raman spectroscopy analysis (Fig. S2), carried out on the samples after subjecting them to calcination at  $500^\circ\text{C}$ , shows that  $\text{Fe}_3\text{O}_4$ @Sr transformed to hematite, while  $\text{Fe}_3\text{O}_4$ @Gd were thermally stable without any trace of transformation. Given this, it can be affirmed that  $\text{Gd}^{3+}$  substitution up to 2.5% stabilizes the crystal structure and magnetic behavior of the nanoferrites while the effect of  $\text{Sr}^{2+}$  could not be felt. According to Cornell and Schwertmann [23], the substitution of Fe with other cations could prevent the thermal transformation of iron oxides from one phase to another. The coercive field  $H_c$  is as low as 5 and 12 Oe for the  $\text{Fe}_3\text{O}_4$ @Gd and  $\text{Fe}_3\text{O}_4$ @Sr - samples, respectively. This feature is advantageous for practical applications.

In Fig. 3A, we presented the thermogram of  $\text{Fe}_3\text{O}_4$ @Gd,  $\text{Fe}_3\text{O}_4$ @Gd@CA and  $\text{Fe}_3\text{O}_4$ @Gd@CA@5-flu (The focus on Gd as dopant was due to the results obtained from the magnetic hyperthermia which was discussed under section 3.2). The sample  $\text{Fe}_3\text{O}_4$ @Gd was relatively stable within the range of the studied temperature ( $0$ – $800^\circ\text{C}$ ), having approximately 4% mass loss for the entire temperature, due to the loss of water. As shown in Fig, there are 3 distinct regions that are related to the decomposition of different organic compounds from  $\text{Fe}_3\text{O}_4$ @Gd@CA and  $\text{Fe}_3\text{O}_4$ @Gd@CA@5-flu. To start with, the first region (i) which occurred between 0 and  $195^\circ\text{C}$  is due to the thermo-desorption of water that was physically and chemically bound to the structure of  $\text{Fe}_3\text{O}_4$ @Gd@CA and  $\text{Fe}_3\text{O}_4$ @Gd@CA@5-flu. This amount to a mass loss of 7% from these two samples. The second region (between 195 and  $332^\circ\text{C}$ ), labeled (II) with a concave shape, having 33% mass loss was due to the thermo-decomposition of citric acid that was used to functionalize the nanoparticles. After  $332^\circ\text{C}$ , the sample  $\text{Fe}_3\text{O}_4$ @Gd@CA became thermally stable, which implies that all the citric acid that was present has been totally decomposed, leaving behind the iron oxide nanoparticles. Region (iii), which is within the range of  $332$ – $442^\circ\text{C}$ , and observable only for the drug-loaded nanoparticles, is due to the thermal decomposition of the loaded drug, 5-fluorouracil (from  $\text{Fe}_3\text{O}_4$ @Gd@CA@5-flu), which is thermally unstable within this

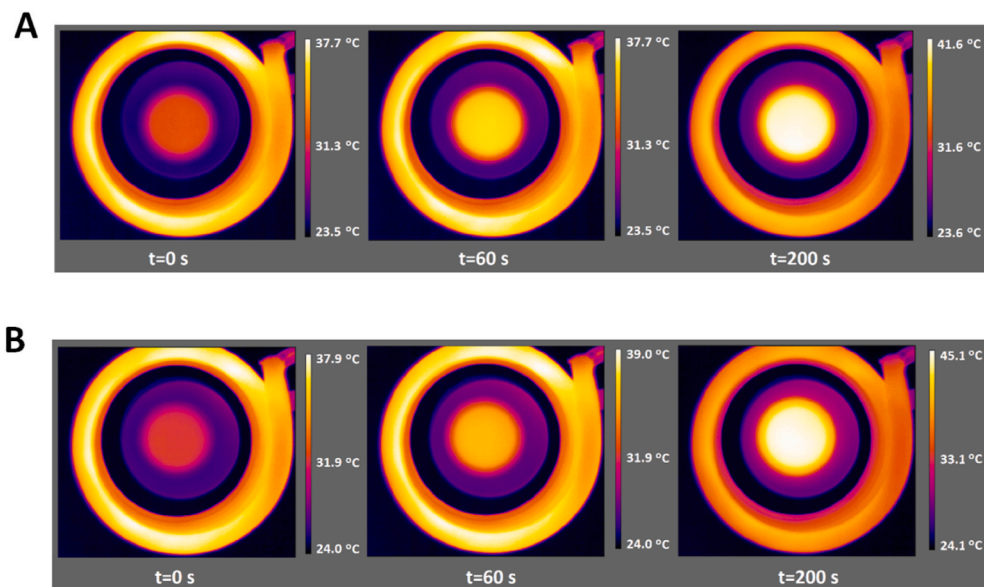


Fig. 4. Images from the thermovision camera on the (A) Fe<sub>3</sub>O<sub>4</sub>@Sr@CA@5-flu and (B) Fe<sub>3</sub>O<sub>4</sub>@Gd@CA@5-flu, where three images reveal the heat distribution before AMF application (left column), after 60 s of 26 G application (middle images), and after 200 s of 26 G application to the sample. The frequency was about 290 kHz.

temperature range. The mass loss in this region is 11%. This implies that 110  $\mu\text{g}$  of the drug is contained in 1 mg of Fe<sub>3</sub>O<sub>4</sub>@Gd@CA@5-flu.

The FTIR spectra of Fe<sub>3</sub>O<sub>4</sub>@Gd@CA and Fe<sub>3</sub>O<sub>4</sub>@Gd@CA@5-flu are shown in Fig. 3B. The spectrum of Fe<sub>3</sub>O<sub>4</sub>@Gd is not shown because it similar to that of undoped magnetite as reported in our previous work [24]. The bands at 549 and 641  $\text{cm}^{-1}$ , on the spectra of the two samples are the characteristics feature of Fe–O in the iron oxide nanoparticles [25]. The presence of 884  $\text{cm}^{-1}$  is related to the C–H out of plane vibration of CF=CH [26]. The peak at 1242  $\text{cm}^{-1}$  is the characteristics of C–F stretching band of 5-fluorouracil [27], whereas the C–H bending vibration appears at 1401  $\text{cm}^{-1}$  [28] at the spectra of both Fe<sub>3</sub>O<sub>4</sub>@Gd@CA and Fe<sub>3</sub>O<sub>4</sub>@Gd@CA@5-flu. The peak at 1622  $\text{cm}^{-1}$  is ascribed to C=O stretching vibration of citric and 5-fluorouracil [28]. The intensity of this peak increase for the spectrum of Fe<sub>3</sub>O<sub>4</sub>@Gd@CA@5-flu which shows that there is interaction between the linker (citric acid) and 5-fluorouracil. This could be interaction of  $\pi$  bond in C=O stretching of citric acid with another  $\pi$  bond in C=O stretching of 5-fluorouracil, known as  $\pi$ - $\pi$  interaction. The shoulder at 3450 and the broad peak at 3149  $\text{cm}^{-1}$  is evidence of the interaction of the drug with the iron oxide nanoparticles doped with gadolinium which could be referred to as hydrogen bond interaction through the oxygen atom of the nanoparticles and the H atom of 5-fluorouracil.

### 3.2. Magnetic hyperthermia analysis

The destruction of cancer cells via hyperthermia treatment is efficient using iron oxides of good magnetic properties and surface functionalization, which are referred in literature to as nanosized heaters [29]. This type of hyperthermia, called localized hyperthermia, involves the heating of as a small area of tissue as required and possible, preferably a tumor. Cancer cells are more sensitive to elevated temperatures than healthy cells and typically they are destroyed at temperatures in the moderate range of 42–46 °C. In this range of temperature, the mechanisms responsible for cell death involve aggregation and denaturation of intracellular proteins. Typically, the heating effect of magnetic nanoparticles shows a dependence on their structural behavior, such as particle confinement, size, and anisotropy [30]. Three mechanisms are responsible for heat generation from magnetic particles. For larger, multi magnetic-domain nanoparticles, the heat generated is due to hysteresis losses. For smaller, below 15 nm diameter superparamagnetic

nanoparticles, that can be considered as single magnetic domain nanoparticles, the heating effect originates from their total magnetic moment which undergoes orientational thermal fluctuations under the influence of an alternating magnetic field (AMF) [31,32]. These fluctuations are due to the internal rotations of the magnetic moment with respect to the crystal lattice of nanoparticles (Néel mechanism) and physical rotations of the whole nanoparticles within the surrounding medium (Brownian mechanism). These two mechanisms are the sources of friction and result in a phase lag between the external magnetic field and the direction of nanoparticles' magnetic moments, generating thermal energy upon the relaxation of magnetization. The Néel and Brownian relaxation times differ, with the former depending strongly on the nanoparticle size and its anisotropy, and the latter depending on the hydrodynamic size of the nanoparticle, but much more on the viscosity of the surrounding medium. Néel relaxation prevails in the higher frequency of an AMF and smaller particle size, whereas Brown's contribution is larger for larger particle size and greater medium viscosity [33]. The overall heat dissipation value depends therefore on the frequency and amplitude of the applied magnetic field and the magnetic properties and size of nanoparticles and is experimentally quantified from the value of specific loss power or specific absorption rate (SAR). The values of SAR are usually determined using Eq. 1

$$SAR = \frac{d C_e}{N_p} \left( \frac{dT}{dt} \right)_{max} \quad 1$$

where the  $d$  is the dispersant density ( $\text{kg m}^{-3}$ );  $C_e$  is a dispersant-specific heat ( $\text{kcal kg}^{-1} \text{C}^{-1}$ );  $N_p$  is the density of magnetic nanoparticles ( $\text{kg m}^{-3}$ );  $T$  is the temperature (°C), and  $t$  is the time (s).

Since Fe<sub>3</sub>O<sub>4</sub>@Sr@CA and Fe<sub>3</sub>O<sub>4</sub>@Gd@CA nanoparticles loaded with a drug (5-fluorouracil) are proposed to be used for cancer treatment via the combination of drug release and an increase in the temperature of the affected cells, heat generation was investigated with the use of magnetic hyperthermia (MH). In these experiments, the aqueous suspensions of Fe<sub>3</sub>O<sub>4</sub>@Sr@CA and Fe<sub>3</sub>O<sub>4</sub>@Gd@CA were treated with an alternating magnetic field (AMF) of controlled frequency and amplitude. The increase in temperature was measured as a function of the amplitude of the magnetic field until the therapeutic temperature (42–46 °C) was achieved. This temperature range is also known as thermal sensitization, in which the cancer cells become more susceptible to other

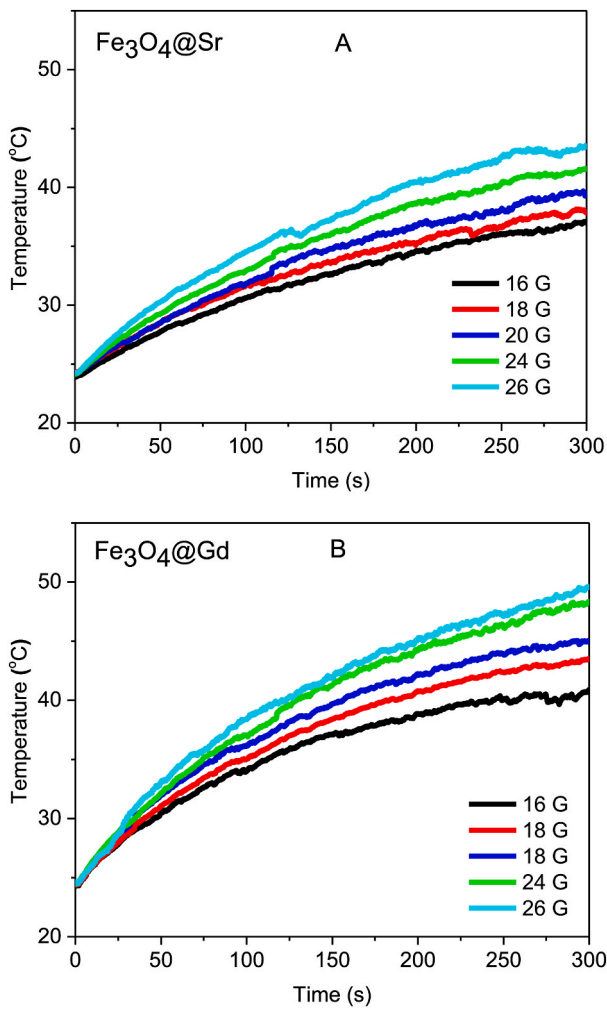


Fig. 5. Temperature change of the different amplitude of AMF for (A) Fe<sub>3</sub>O<sub>4</sub>@Sr@CA@5-flu and (B) Fe<sub>3</sub>O<sub>4</sub>@Gd@CA@5-flu, where the concentration was 10 mg mL<sup>-1</sup>.

treatment techniques (that is a combination of hyperthermia and drug delivery [34]). Whenever the elevated temperature of the tissue is above the physiological level, there will be changes in the vascular permeability, an increase in the blood flow, which eventually resulted in the oxygenation of the tumor [35].

To start with, the images of the suspension of Fe<sub>3</sub>O<sub>4</sub>@Sr@CA and

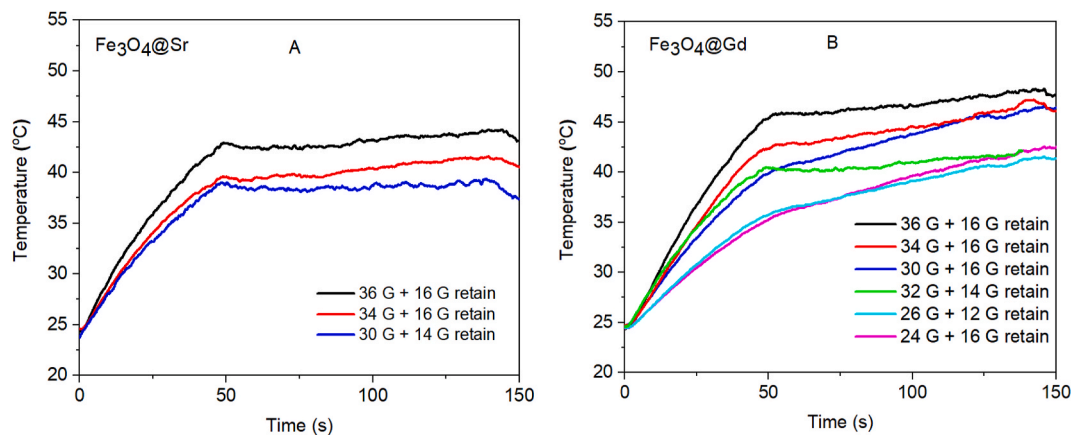


Fig. 6. Temperature change of the different amplitude of AMF with the retain pulses above 50 s for (A) Fe<sub>3</sub>O<sub>4</sub>@Sr@CA@5-flu and (B) Fe<sub>3</sub>O<sub>4</sub>@Gd@CA@5-flu, where the concentration was 10 mg mL<sup>-1</sup>.

Fe<sub>3</sub>O<sub>4</sub>@Gd@CA during heating were recorded using a thermovision camera (Fig. 4). The following Fig. 4A and B show the images recorded using a thermovision camera for Fe<sub>3</sub>O<sub>4</sub>@Sr@CA@5-flu and Fe<sub>3</sub>O<sub>4</sub>@Gd@CA@5-flu, respectively. Suspensions were kept in the center of the magnetic field generating coil on a Petri dish and subject to thermal imaging before and during AMF application, particularly after 60 s and 200 s measurements. The amplitude was about 26 G, and the frequency was 290 kHz. It is clearly seen that the suspensions heat uniformly during the heat generation. For these parameters ( $H_0 = 26$  G and  $f = 290$  kHz) the Hof is about  $5.95 \times 10^8$  Am<sup>-1</sup>s<sup>-1</sup> and is slightly above the Atkinson-Brezovich safety limit Hof <  $4.85 \times 10^8$  Am<sup>-1</sup>s<sup>-1</sup> ( $6 \times 10^6$  Oe Hz) [36]. However, another work shows a higher acceptable limit Hof <  $5.0 \times 10^9$  Am<sup>-1</sup>s<sup>-1</sup> ( $25 \times 10^7$  Oe Hz) making the proposed conditions suitable to be applied in the small body regions [37].

In this (MH) analysis, the suspension of Fe<sub>3</sub>O<sub>4</sub>@Sr@CA@5-flu and Fe<sub>3</sub>O<sub>4</sub>@Gd@CA@5-flu with a density of about 10 mg L<sup>-1</sup> was placed in a Petri-dish and then, in the coil generating AMF. The AMF frequency was about 290 kHz and its magnitude was applied in the range of 16–36 G. The heat generation was recorded with the thermovision camera. Fig. 5A and B show the plots of the increase of temperature in time, for Fe<sub>3</sub>O<sub>4</sub>@Sr@CA@5-flu and Fe<sub>3</sub>O<sub>4</sub>@Gd@CA@5-flu, respectively, at different AMF intensities. These results (Fig. 5A and B), show that the nano heater, Fe<sub>3</sub>O<sub>4</sub>@Sr@CA@5-flu heated up at a slower rate compared to Fe<sub>3</sub>O<sub>4</sub>@Gd@CA@5-flu. The presence of seven unpaired electrons in Gd<sup>3+</sup> in Fe<sub>3</sub>O<sub>4</sub> that retained its magnetic properties at higher temperatures could have led to its ability to generate more heat in the alternating magnetic field than Sr<sup>2+</sup> with no unpaired electrons.

As discussed above, the heat generation mediated by magnetic nanoparticles in the presence of an external AMF can be quantified by the value of specific loss power, also named as specific absorption rate (SAR). One of the requirements for superparamagnetic iron oxide nanoparticles suitability for hyperthermia treatment is that they must have a high specific absorption rate (SAR) so that lower dose of the nanoparticles and lower values of the product of magnetic field strength and frequency will be used during the application [38]. Therefore, the specific absorption rate (SAR) was determined using Eq. (1).

The calculated SAR values are about  $112.0 \pm 10.4$  W g<sup>-1</sup> for Fe<sub>3</sub>O<sub>4</sub>@Gd@CA@5-flu at 26 G, while that of Fe<sub>3</sub>O<sub>4</sub>@Sr@CA@5-flu ranges from  $92.0 \pm 11.3$  W g<sup>-1</sup> at 26 G. These values are higher than  $66 \pm 18$  that was reported for Fe<sub>3</sub>O<sub>4</sub> + Dx-ECH-Amine-CREKA by Anastasia et al. [39]. The observed lower value of the SAR for Sr-based carriers can be related to the dopant's valency. It has been reported that the incorporation of Co (with three unpaired electrons) into the ferrite structure resulted in an increase in SAR value [40]. Therefore, the higher values of SAR doped with Gd<sup>3+</sup> as reported in this study could be due to the availability of unpaired electrons upon substitution of part of Fe<sup>3+</sup>

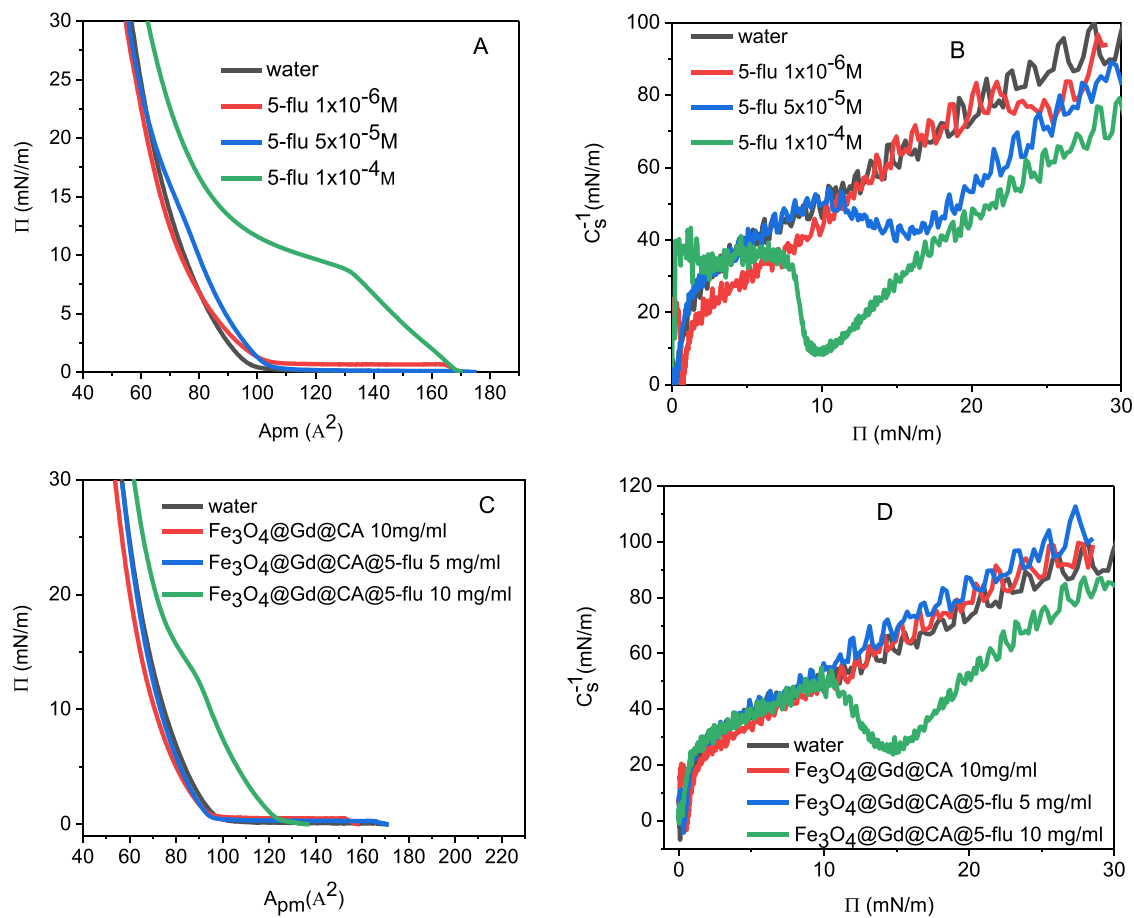


**Fig. 7.** Langmuir isotherms (A, C) and reciprocal of the compression modulus vs surface pressure plots (B, D) of mixed lipids DOPC:DOPS (in molar ratio 0.8:0.2). The composition of the subphase described in the legend.

cations. When the value of SAR is high, it implies that the residence time of the nanoparticles in the human body is low, this will lead to a lower amount of the nanoparticles that will be administered to the cancer patient [38]. This implies that the amount of  $\text{Fe}_3\text{O}_4@Gd@CA@5-flu$  that will be administered into the human body will be lower than that of  $\text{Fe}_3\text{O}_4@Sr@CA@5-flu$ .

From the medical point of view the sample should reach a plateau at the temperature in the range of 42–46 °C (mild hyperthermia) and keep it constant for several minutes to achieve the desired effect in cancer treatment. Therefore, based on the results obtained for the single pulse MH and the SAR values, the following measurement was performed with the pulse change, where the higher amplitude of AMF was initially applied. Then, when the sample was heated up to therapeutic values of 42–46 °C, the subsequent retain pulse with a lower amplitude of AMF was applied. As can be seen in Fig. 6A and B for  $\text{Fe}_3\text{O}_4@Sr@CA@5-flu$  and  $\text{Fe}_3\text{O}_4@Gd@CA@5-flu$  respectively, depending on the applied amplitude of AMF, the desired temperature can be controlled with the change of the pulse.

A similar approach to mitigate the side effects of magnetic nanoparticle hyperthermia by the intermittent, pulse magnetic field application was proposed in the case of cancer tissue phantom, resulting in the temperature variations of healthy tissue phantom well below 4 °C [41].

The amplitude of AMF applied to the Sr-doped carriers needs to be higher than for Gd-doped carriers. In comparison to the single pulse, the desired temperature can be reached much faster for both suspensions. Applying the AMF in a pulse mode enables fast generation of the heat with a therapeutic temperature range, shortening the treatment time, fast drug delivery, and reducing the AMF conditions, making it safe for

patient treatment. It is worth mentioning that SAR values and the trend of the T-t curves in AMF are similar due to the high colloidal stability and narrow size distribution of magnetic nanocarriers, similar to the results presented in the literature [42]. For the initial 36 G at initial 50 s the Hof is about  $8.25 \times 10^8 \text{ Am}^{-1}\text{s}^{-1}$  and then, the amplitudes below 21.5 G give the Hof below the Atkinson-Brezovich limit making it suitable for the safe treatment.

Since  $\text{Fe}_3\text{O}_4@Gd@CA@5-flu$  showed better results for the MH, higher value of SAR, and Fe cation substitution based on the magnetic saturation and Raman spectroscopy analysis, further studies were carried out on these nanoparticles.

### 3.3. The interactions of the nanoparticles with biomimetic membranes

The Langmuir technique is one of the most precise and simple methods to obtain well-ordered monolayers that can imitate the structure and composition of biomembranes. The composition of monolayers can be controlled by mixing the components in a certain proportion. This allows the preparation of several different types of membranes that can serve as an excellent model of biomembranes. To gain deeper insight into the interactions of nanoparticle- 5-flu drug conjugates with the cancer cell membranes, as a first step of our studies, we present the effect of the conjugate on the organization of Langmuir lipid film that mimics the lipidic content of cancer cells.

For Langmuir's experiments, a mixture of DOPC:DOPS lipids (in a molar ratio of 0.8:0.2) was used. Lipids with the choline moiety are the most abundant compounds in the membranes of eukaryotic cells. Phosphocholine with a *cis*-9 double bond, such as DOPC (1,2-dioleoyl-sn-glycero-3) represents a major fraction of all biomembranes. The other

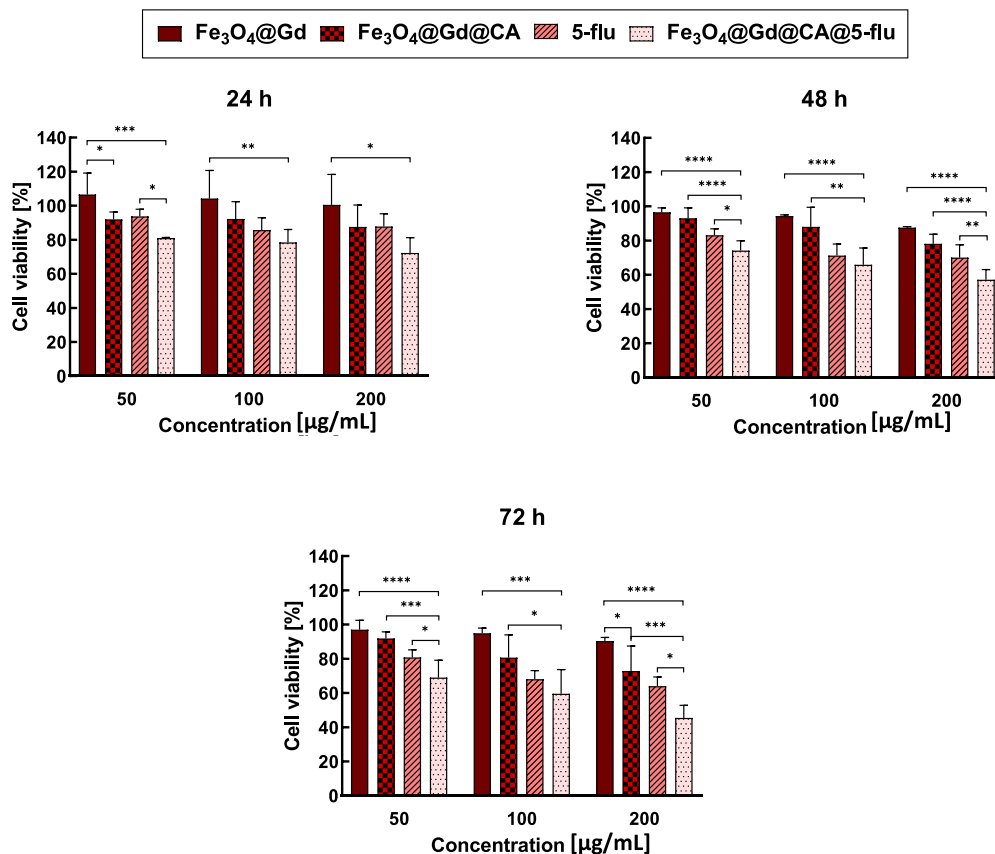


Fig. 8. Cytotoxicity studies of Fe<sub>3</sub>O<sub>4</sub>@Gd, Fe<sub>3</sub>O<sub>4</sub>@Gd@CA, 5-flu, Fe<sub>3</sub>O<sub>4</sub>@Gd@CA@5-flu compounds performed on SKOV-3 cells. Data are expressed as  $\pm$  SD (n = 3). Statistical significance was considered if  $p < 0.05$  (\*),  $p < 0.01$  (\*\*),  $p < 0.001$  (\*\*\*), and  $p < 0.0001$  (\*\*\*\*).

of the used lipids, DOPS (1,2-dioleoyl-sn-glycero-3-phospho-L-serine), is mainly enriched in the intracellular layer of the cell membrane. Its content in the biomembranes is estimated to be in the range of 6–20 mol % [43]. However, phosphatidylserine may be considered a tumor marker because in cancer cells the molecules of DOPS pass to the outer layer of the membrane [44].

The presented studies were performed for the conjugate (Fe<sub>3</sub>O<sub>4</sub>@Gd@CA@5-flu) and, separately, on its components (5-fluorouracil and Fe<sub>3</sub>O<sub>4</sub>@Gd@CA). For each of the systems system a Langmuir isotherm, called the  $\pi$ -A plot, was recorded. Next, to analyze the effect of the presence of nanoparticles on molecular packing in the monolayer in more detail, the reciprocal of the compression modulus values  $C_s^{-1}$ , were calculated directly from the isotherm data using equation (2).

$$C_s^{-1} = -A \left( \frac{d\pi}{dA} \right) \quad 2$$

where: A-area per lipid molecule in the monolayer;  $\Pi$ -surface pressure.

The results show the correlation between the concentration of the free drug added to the subphase and the effect of the membrane packing. Based on the isotherms, the concentration range of  $1 \times 10^{-6}$  M up to  $1 \times 10^{-5}$  M of 5-fluorouracil has no effect on the membrane structure (Fig. 7A). A 10-fold increase in the concentration of 5-fluorouracil causes significant changes in the organization of lipids. At that concentration, the drug strongly adsorbs on the mixed monolayer surface, particularly at low values of surface pressure (Fig. 7B; green curve). With further compression above  $10 \text{ mN m}^{-1}$ , a large amount of the therapeutic is suddenly squeezed out of the surface of the monolayer. It is visible as a plateau in the green curve. The isotherm recorded for the drug is shifted in relation to the curve for lipids on the water even for higher surface pressure, which confirms the penetration of the drug

molecules into the monomolecular film. Further, these observations are supported by the values of the reciprocal of compressibility modulus (Fig. 7B). The  $C_s$  value of the pure lipids monolayers equals  $100 \text{ mN m}^{-1}$ ; it is in agreement with literature data and close to the values for the liquid expanded (LE;  $12\text{--}100 \text{ mN m}^{-1}$ ) and liquid-condensed (LC;  $100\text{--}250 \text{ mN m}^{-1}$ ) phases. For the subphase containing a higher concentration of 5-fluorouracil, the  $C_s$  value decreases to about  $70 \text{ mN m}^{-1}$ , due to the change in the phase state of a monolayer. At the same time, at  $\Pi = 10 \text{ mN m}^{-1}$ , there is a minimum on the curve, which suggests a relationship between drug adsorption and the process of membrane compression (squeezing out the drug off the surface of the monolayer at  $p = 10 \text{ mN m}^{-1}$ ).

In the next step, solutions of Fe<sub>3</sub>O<sub>4</sub>@Gd@CA and Fe<sub>3</sub>O<sub>4</sub>@Gd@CA@5-flu with different concentrations were used as sub-phases (Fig. 7C and D). The results show that the addition of nanoparticles modified by citric acid, regardless of their concentration, does not affect the structure of the layer. That proves that the carrier is neutral in relation to the biomimetic membrane. In vitro tests (*vide infra*) confirm the lack of cytotoxicity of the nanoparticles toward the human ovarian cancer cell line (SKOV-3 cells). This result stays in agreement with previous studies on the interactions of nanoparticles with lipid monolayers [25,45].

Modification of nanostructures with fluorouracil changes the surface properties of the nanocarrier. The isotherms show that the concentration of the conjugate at the level of  $10 \text{ mg ml}^{-1}$  (corresponding to the amount of free drug in the subphase of ca.  $8 \times 10^{-6}$  M) significantly affects the shape of the curve. The value of the compressibility factor in the presence of high conjugate concentrations ( $10 \text{ mg L}^{-1}$ ) reveals a marked decrease of  $C_s$  with a characteristic minimum at  $\Pi = 15 \text{ mN m}^{-1}$ . These changes confirm the lipid reorganization caused by the addition of the

**Table 1**  
Drug-loaded magnetic nanocarriers for cancer cell death.

| Magnetic carrier                          | Antitumor drugs | Tumor cell lines | % cell death after | References |
|---|-----------------|------------------|--------------------|------------|
| LSMO-Fe <sub>3</sub> O <sub>4</sub>       | Paclitaxel      | MCF-7            | 24                 | [46]       |
| PMMA-Fe <sub>3</sub> O <sub>4</sub> -PAA  | Doxorubicin     | 4 T1             | 34                 | [47]       |
| Ferumoxytol-medical chitosan              | Doxorubicin     | HT-29            | 17.8               | [48]       |
| Silica-Fe <sub>3</sub> O <sub>4</sub>     | Maytansinoid    | IC21             | 15                 | [49]       |
| Oleosome-ZnFe <sub>2</sub> O <sub>4</sub> | Carmustine      | SK-BR-3          | 40                 | [50]       |
| Fe <sub>3</sub> O <sub>4</sub> @Gd        | 5-Fluorouracil  | SKOV-3           | 55                 | This work  |

drug. Similar changes in the presence of free drug are revealed only at higher concentrations of the therapeutic, i.e., at ca. 10<sup>-4</sup> M. Carrier-bound fluorouracil seems to accumulate more strongly in the membrane, which may explain the greater cytotoxicity of the conjugate compared to the free drug towards SKOV-3 cell lines (see below).

### 3.4. *In-vitro* cytotoxic effect of the nanoparticles

The cytotoxic effect of Fe<sub>3</sub>O<sub>4</sub> doped gadolinium was tested on a human ovarian cancer cell line with epithelial-like morphology (SKOV-3 cells) using an MTS assay. Based on the obtained results, as shown in Fig. 8, Fe<sub>3</sub>O<sub>4</sub>@Gd proved to be non-toxic at the three various concentrations (50, 100, and 200 μM) after 24 h of incubation time. Meanwhile, an approximate 5% slight decrease in the viable cells was observed after 48 and 72 h of incubation time. However, considering the results for Fe<sub>3</sub>O<sub>4</sub>@CA@5-flu, it exhibits cytotoxicity to the SKOV-3 cells in a time and concentration-dependent manner. After 72 h and at 50 μM of Fe<sub>3</sub>O<sub>4</sub>@CA@5-flu concentration average of 30% of the cells were observed as dead. When the concentration was increased to 200 μM, only 45% of cells were metabolically active. A shorter incubation time caused lower cytotoxicity of Fe<sub>3</sub>O<sub>4</sub>@CA@5-flu. Furthermore, the viability of SKOV-3 cells treated with Fe<sub>3</sub>O<sub>4</sub>@CA@5-flu was lower in comparison to Fe<sub>3</sub>O<sub>4</sub>@CA@ and free 5-flu at the same concentrations. Although ca. 110 μg of 5-flu was successfully loaded on Fe<sub>3</sub>O<sub>4</sub>@CA@5-flu, high efficiency in the reduction of cancer cells viability was achieved. To summarize, the obtained results confirm the potential of Fe<sub>3</sub>O<sub>4</sub>@Gd nanoparticles to enhance 5-flu anticancer efficacy.

The comparison of the effectiveness of Fe<sub>3</sub>O<sub>4</sub>@CA@5-flu in destroying cancer cells was itemized in Table 1. The table shows that our nanoparticles drug-carrier is more effective than some reported work in the literature.

## 4. Conclusion

In this study, iron oxide nanoparticles (magnetite) doped with strontium (Sr<sup>2+</sup>) and gadolinium (Gd<sup>3+</sup>) were produced and applied for the delivery of 5-fluorouracil for ovarian cancer (SKOV-3 cells) therapy. There is no difference between the magnetic saturation values of the as-received (without thermal treatment) Fe<sub>3</sub>O<sub>4</sub>@Sr and Fe<sub>3</sub>O<sub>4</sub>@Gd. The response of suspension of Fe<sub>3</sub>O<sub>4</sub>@Gd modified with citric acid, and loaded with the antitumor agent (Fe<sub>3</sub>O<sub>4</sub>@Gd@CA@5-flu) to heat generation in an alternating magnetic field for the application of magnetic hyperthermia, was faster than of Fe<sub>3</sub>O<sub>4</sub>@Sr@CA@5-flu. This was assumed to be due to the ability of Gd<sup>3+</sup> to replace part of the Fe ions which Sr<sup>2+</sup> could not achieve as proven by the Raman and magnetic saturation values of the thermally treated doped nanoparticles. Langmuir technique shows that the nanoparticles (Fe<sub>3</sub>O<sub>4</sub>@Sr@CA@5-flu) interacted with biological membrane analogs. Preliminary cytotoxicity studies indicated that Fe<sub>3</sub>O<sub>4</sub>@Gd nanoparticles are potentially promising candidates for drug (5-flu) carriers leading to a significant reduction in the metabolism activity of the cancer cells and finally, in the future, tumor progression. Nevertheless, further *in vitro* as well as *in vivo* experiments are needed to approve the anticancer efficacy of

Fe<sub>3</sub>O<sub>4</sub>@CA@5-flu.

## Declaration of competing interest

The authors declare that they have no known competing financial interests or personal relationships that could have appeared to influence the work reported in this paper.

## Acknowledgments

Sunday J. Olusegun with No PPN/U/LM/2020/1/00051/DEC/01, would like to thank the NAWA - Narodowa Agencja Wymiany Akademickiej (Polish National Agency for Academic Exchange) for their support.

## Appendix A. Supplementary data

Supplementary data to this article can be found online at <https://doi.org/10.1016/j.ceramint.2023.03.102>.

## References

- [1] S.M. M., S. Veerananarayanan, T. Maekawa, S.K. D., External stimulus responsive inorganic nanomaterials for cancer theranostics, *Adv. Drug Deliv. Rev.* 138 (2019) 18–40, <https://doi.org/10.1016/j.addr.2018.10.007>.
- [2] R.D. Dolan, B.J.A. Laird, P.G. Horgan, D.C. Mcmillan, The prognostic value of the systemic inflammatory response in randomised clinical trials in cancer : a systematic review, *Crit. Rev. Oncol. Hematol.* 132 (2018) 130–137, <https://doi.org/10.1016/j.critrevonc.2018.09.016>.
- [3] J. Zhou, Z. Huang, U. Kumar, D.D.Y. Chen, Review of recent developments in determining volatile organic compounds in exhaled breath as biomarkers for lung cancer diagnosis, *Anal. Chim. Acta* 996 (2017) 1–9, <https://doi.org/10.1016/j.aca.2017.09.021>.
- [4] X. Zhang, H. Xiao, Y. Chen, Effects of life review on mental health and well-being among cancer patients : a systematic review, *Int. J. Nurs. Stud.* 74 (2017) 138–148, <https://doi.org/10.1016/j.ijnurstu.2017.06.012>.
- [5] R.C.R. Apostolos, M.C. De Miranda, W.M. Silva, D. de A. Gomes, M.C. de Miranda, E.M.B. de Sousa, Hybrid polymeric systems of mesoporous silica/hydroxyapatite nanoparticles applied as antitumor drug delivery platform, *Int. J. Appl. Ceram. Technol.* 16 (2019) 1836–1849, <https://doi.org/10.1111/ijac.13231>.
- [6] S. Shirvalilou, S. Khoei, S. Khoei, N. Jamali, Development of a magnetic nanographene oxide carrier for improved glioma-targeted drug delivery and imaging : *in vitro* and *in vivo* evaluations, *Chem. Biol. Interact.* 295 (2018) 97–108, <https://doi.org/10.1016/j.cbi.2018.08.027>.
- [7] M.S. Dahiya, V.K. Tomer, S. Duhan, Metal–ferrite nanocomposites for targeted drug delivery, *Appl. Nanocomposite Mater. Drug Deliv.* (2018), <https://doi.org/10.1016/B978-0-12-813741-3.00032-7>, 0–24.
- [8] S. Jafari, A. Akbar, S. Hosnieh, T. Payam, H. Mojtaba, Optimization and development of drug loading in hydroxyapatite – polyvinyl alcohol nanocomposites via response surface modeling approach, *J. Iran. Chem. Soc.* 17 (2020) 1141–1151, <https://doi.org/10.1007/s13738-019-01841-w>.
- [9] K. Yu, M. Liu, H. Dai, Targeted drug delivery systems for bladder cancer therapy, *J. Drug Deliv. Sci. Technol.* 56 (2020), 101535, <https://doi.org/10.1016/j.jddst.2020.101535>.
- [10] X. Kang, H. Chen, S. Li, L. Jie, J. Hu, X. Wang, J. Qi, X. Ying, Y. Du, Magnesium lithospermate B loaded PEGylated solid lipid nanoparticles for improved oral bioavailability, *Colloids Surf. B Biointerfaces* 161 (2018) 597–605, <https://doi.org/10.1016/j.colsurfb.2017.11.008>.
- [11] N. D. S.R. Chetna Dhand, Molamma P. Prabhakaran, Roger W. Beuerman, R. Lakshminarayanan, Role of size of drug delivery carriers for pulmonary and intravenous administration with emphasis on cancer therapeutics and lung-targeted drug delivery, *RSC Adv.* 4 (2014) 32673–32689, <https://doi.org/10.1039/c4ra02861a>.
- [12] X. Fang, J. Cao, A. Shen, Advances in anti-breast cancer drugs and the application of nano-drug delivery systems in breast cancer therapy, *J. Drug Deliv. Sci. Technol.* 57 (2020), 101662, <https://doi.org/10.1016/j.jddst.2020.101662>.
- [13] Y. Lu, E. Zhang, J. Yang, Z. Cao, Strategies to improve micelle stability for drug delivery, *Nano Res.* 11 (2018) 4985–4998.
- [14] S. Palanisamy, Y. Wang, Superparamagnetic iron oxide nanoparticulate system: synthesis, targeting, drug delivery and therapy in cancer, *Dalton Trans.* 48 (2019), <https://doi.org/10.1039/c9dt00459a>.
- [15] R. Aleksandra, G. Cichowicz, M.K. Cyranski, P. Marek, P. Kryszynski, Synthesis and characterization of Gd<sup>3+</sup> and Tb<sup>3+</sup>-doped iron oxide nanoparticles for possible endoradiotherapy and hyperthermia, *J. Magn. Magn. Mater.* 479 (2019) 50–58, <https://doi.org/10.1016/j.jmmm.2019.01.102>.
- [16] S. Pors Nielsen, The biological role of strontium, *Bone* 35 (2004) 583–588, <https://doi.org/10.1016/j.bone.2004.04.026>.
- [17] L. He, G. Dong, C. Deng, Effects of strontium substitution on the phase transformation and crystal structure of calcium phosphate derived by chemical

- precipitation, *Ceram. Int.* 42 (2016) 11918–11923, <https://doi.org/10.1016/j.ceramint.2016.04.116>.
- [18] O.I. Ebenezer, A.L. Abdul, N.S. Fazliani, I. Suzylawati, Gadolinium based contrast agents (GBCAs): uniqueness, aquatic toxicity concerns, and prospective remediation, *J. Contam. Hydrol.* 250 (2022), 104057, <https://doi.org/10.1016/j.jconhyd.2022.104057>.
- [19] R.D. Teo, J. Termini, H.B. Gray, Lanthanides: applications in cancer diagnosis and therapy, *J. Med. Chem.* 59 (2017) 6012–6024, <https://doi.org/10.1021/acs.jmedchem.5b01975.Lanthanides>.
- [20] D.K. Chatterjee, P. Diagaradjane, S. Krishnan, Nanoparticle-mediated hyperthermia in cancer therapy, *Ther. Deliv.* 2 (2011) 1001–1014, <https://doi.org/10.4155/tde.11.72>.
- [21] M. Thommes, K. Kaneko, A.V. Neimark, J.P. Olivier, F. Rodriguez-Reinoso, J. Rouquerol, K.S.W. Sing, Physisorption of gases, with special reference to the evaluation of surface area and pore size distribution (IUPAC Technical Report), *Pure Appl. Chem.* 87 (2015) 1051–1069, <https://doi.org/10.1515/pac-2014-1117>.
- [22] S.J. Olusegun, N.D.S. Mohalle, Insight into the adsorption of doxycycline hydrochloride on different thermally treated hierarchical CoFe<sub>2</sub>O<sub>4</sub>/bio-silica nanocomposite, *J. Environ. Chem. Eng.* 7 (2019), 103442, <https://doi.org/10.1016/j.jece.2019.103442>.
- [23] R.M. Cornell, U. Schwertmann, *The Iron Oxides. Structure, Properties, Reactions, Occurrences and Uses*, second ed., Wiley-VCH Verlag GmbH & Co. KGaA, 2003.
- [24] A. Rekorajska, G. Cichowicz, M.K. Cyranski, M. Pękala, P. Krysiński, Synthesis and characterization of Gd<sup>3+</sup> and Tb<sup>3+</sup>-doped iron oxide nanoparticles for possible endoradiotherapy and hyperthermia, *J. Magn. Magn. Mater.* 479 (2019) 50–58, <https://doi.org/10.1016/j.jmmm.2019.01.102>.
- [25] D. Nieciecka, A. Rekorajska, D. Cichy, P. Końska, M. Żuk, P. Krysiński, Synthesis and characterization of magnetic drug carriers modified with Tb<sup>3+</sup> ions, *Nanomaterials* 12 (2022) 795, <https://doi.org/10.3390/nano12050795>.
- [26] E.A.K. Nivethaa, S. Dhanavel, V. Narayanan, C.A. Vasu, A. Stephen, An in vitro cytotoxicity study of 5-fluorouracil encapsulated chitosan/gold nanocomposites towards MCF-7 cells, *RSC Adv.* 5 (2015) 1024–1032, <https://doi.org/10.1039/c4ra11615a>.
- [27] M. Olukman, O. Şanlı, E.K. Solak, Release of anticancer drug 5-fluorouracil from different ionically crosslinked alginate beads, *J. Biomaterials Nanobiotechnol.* (2012) 469–479, <https://doi.org/10.4236/jbnb.2012.34048>, 03.
- [28] A.M. Mohammed, S.K. Osman, K.I. Saleh, A.M. Samy, In vitro release of 5-fluorouracil and methotrexate from different thermosensitive chitosan hydrogel systems, *AAPS PharmSciTech* 21 (2020) 1–11, <https://doi.org/10.1208/s12249-020-01672-6>.
- [29] M. Bañobre-López, A. Teijeiro, J. Rivas, Magnetic nanoparticle-based hyperthermia for cancer treatment, *Reports Pract. Oncol. Radiother.* 18 (2013) 397–400, <https://doi.org/10.1016/j.rpor.2013.09.011>.
- [30] M.E. Sadat, R. Patel, J. Sookoor, S.L. Bud'Ko, R.C. Ewing, J. Zhang, H. Xu, Y. Wang, G.M. Pauletti, D.B. Mast, D. Shi, Effect of spatial confinement on magnetic hyperthermia via dipolar interactions in Fe<sub>3</sub>O<sub>4</sub> nanoparticles for biomedical applications, *Mater. Sci. Eng., C* 42 (2014) 52–63, <https://doi.org/10.1016/j.msec.2014.04.064>.
- [31] J. Carrey, B. Mehdaoui, M. Respaud, Simple models for dynamic hysteresis loop calculations of magnetic single-domain nanoparticles: application to magnetic hyperthermia optimization, *J. Appl. Phys.* 109 (2011), <https://doi.org/10.1063/1.3551582>.
- [32] M. Lévy, C. Wilhelm, J.M. Siaugue, O. Horner, J.C. Bacri, F. Gazeau, Magnetically induced hyperthermia: size-dependent heating power of  $\gamma$ -Fe<sub>2</sub>O<sub>3</sub> nanoparticles, *J. Phys. Condens. Matter* 20 (2008), <https://doi.org/10.1088/0953-8984/20/20/204133>, 0–5.
- [33] P. Das, M. Colombo, D. Prosperi, Recent advances in magnetic fluid hyperthermia for cancer therapy, *Colloids Surf. B Biointerfaces* 174 (2019) 42–55, <https://doi.org/10.1016/j.colsurfb.2018.10.051>.
- [34] J. Beik, Z. Abed, F.S. Ghoreishi, S. Hosseini-Nami, S. Mehrzadi, A. Shakeri-Zadeh, S.K. Kamrava, Nanotechnology in hyperthermia cancer therapy: from fundamental principles to advanced applications, *J. Contr. Release* 235 (2016) 205–221, <https://doi.org/10.1016/j.jconrel.2016.05.062>.
- [35] Z. Vujaskovic, C.W. Song, Physiological mechanisms underlying heat-induced radiosensitization, *Int. J. Hyperther.* 20 (2004) 163–174, <https://doi.org/10.1080/02656730310001619514>.
- [36] R. Hergt, R. Hiergeist, I. Hilger, W.A. Kaiser, Y. Lapatinikov, S. Margel, U. Richter, Maghemite nanoparticles with very high AC-losses for application in RF-magnetic hyperthermia, *J. Magn. Magn. Mater.* 270 (2004) 345–357, <https://doi.org/10.1016/j.jmmm.2003.09.001>.
- [37] I.M. Obaidat, V. Narayanaswamy, S. Alaabed, S. Sambasivam, C.V.V. Muralee Gopi, Principles of magnetic hyperthermia: a focus on using multifunctional hybrid magnetic nanoparticles, *Magnetochemistry* 5 (2019), <https://doi.org/10.3390/magnetochemistry5040067>.
- [38] K. Kekalo, I. Baker, R. Meyers, J. Shyong, Magnetic nanoparticles with high specific absorption rate at low alternating magnetic field, *Nano Life* 9 (2015) 1–13, <https://doi.org/10.1142/S1793984415500026>.
- [39] A.M. Kruse, S.A. Meenach, K.W. Anderson, J.Z. Hilt, Synthesis and characterization of CREKA-conjugated iron oxide nanoparticles for hyperthermia applications, *Acta Biomater.* 10 (2014) 2622–2629, <https://doi.org/10.1016/j.actbio.2014.01.025>.
- [40] K.A. Kekalo, B.E. Kashevsky, V.E. Agabekov, S.B. Kashevsky, I.V. Prokhorov, G. K. Zhavnerko, Influence of Co amount on the efficiency of energy absorption of Fe-Co ferrite nanoparticles, *J. Magn. Magn. Mater.* 321 (2009) 1514–1516, <https://doi.org/10.1016/j.jmmm.2009.02.076>.
- [41] A.R. Tsiapla, A.A. Kalimeri, N. Maniotis, E. Myrovali, T. Samaras, M. Angelakeris, O. Kalogirou, Mitigation of magnetic particle hyperthermia side effects by magnetic field controls, *Int. J. Hyperther.* 38 (2021) 511–522, <https://doi.org/10.1080/02656736.2021.1899310>.
- [42] K.C. Barick, P.A. Hassan, Glycine passivated Fe<sub>3</sub>O<sub>4</sub> nanoparticles for thermal therapy, *J. Colloid Interface Sci.* 369 (2012) 96–102, <https://doi.org/10.1016/j.jcis.2011.12.008>.
- [43] W. Szlasa, I. Zendran, A. Zalesińska, M. Tarek, J. Kulbacka, Lipid composition of the cancer cell membrane, *J. Bioenerg. Biomembr.* 52 (2020) 321–342, <https://doi.org/10.1007/s10863-020-09846-4>.
- [44] R.A. Chaurio, C. Janko, L.E. Muñoz, B. Frey, M. Herrmann, U.S. Gaipl, Phospholipids: key players in apoptosis and immune regulation, *Molecules* 14 (2009) 4892–4914, <https://doi.org/10.3390/molecules14124892>.
- [45] D. Nieciecka, J. Celej, M. Żuk, A. Majkowska-pilip, K. Żelechowska-matysiak, A. Lis, M. Osial, Hybrid system for local drug delivery and magnetic hyperthermia based on spions loaded with doxorubicin and epirubicin, *Pharmaceutics* 13 (2021), <https://doi.org/10.3390/pharmaceutics13040480>.
- [46] M. Gogoi, H.D. Sarma, D. Bahadur, R. Banerjee, Biphasic magnetic nanoparticles–nanovesicle hybrids for chemotherapy and self-controlled hyperthermia, *Nanomedicine* 9 (2013) 955–970.
- [47] L. Xie, W. Jin, X. Zuo, S. Ji, W. Nan, H. Chen, S. Gao, Q. Zhang, Construction of small-sized superparamagnetic Janus nanoparticles and their application in cancer combined chemotherapy and magnetic hyperthermia, *Biomater. Sci.* 8 (2020) 1431–1441, <https://doi.org/10.1039/c9bm01880h>.
- [48] B. Chen, J. Xing, M. Li, Y. Liu, M. Ji, DOX@Ferumoxytol-Medical Chitosan as magnetic hydrogel therapeutic system for effective magnetic hyperthermia and chemotherapy in vitro, *Colloids Surf. B Biointerfaces* 190 (2020), 110896, <https://doi.org/10.1016/j.colsurfb.2020.110896>.
- [49] S. Ullah, K. Seidel, S. Türkkan, D.P. Warwas, T. Dubich, M. Rohde, H. Hauser, P. Behrens, A. Kirschning, D. Mario Köster, Macrophage entrapped silica coated superparamagnetic iron oxide particles for controlled drug release in a 3D cancer model, *J. Contr. Release* 294 (2019) 327–336.
- [50] H.Y. Cho, T. Lee, J. Yoon, Z. Han, H. Rabie, K.B. Lee, W.W. Su, J.W. Choi, Magnetic oleosome as a functional lipophilic drug carrier for cancer therapy, *ACS Appl. Mater. Interfaces* 10 (2018) 9301–9309, <https://doi.org/10.1021/acsami.7b19255>.